REVIEW

Check for updates

Electronic paramagnetic resonance analysis of point defects in lithium niobate: progress and prospects

Huaize Qin,[a] Xu Chen,[a] Jiankang Zhang,[a] Yukun Song,[a] Longxi Zhang,[a] Qilu Liu,[a] Fulei Wang,*[b] Dongzhou Wang, [ID] *[b] Yuanhua Sang [ID] *[a] and Hong Liu [ID] [ab]

Lithium niobate ($LiNbO_3$) crystals, renowned for their exceptional piezoelectric, electro-optic, and nonlinear optical properties, are indispensable in photonic applications such as optical communication, integrated optics, and laser technology. However, the performance of $LiNbO_3$-based devices is fundamentally limited by point defects. Consequently, elucidating the mechanisms underlying point defect formation and achieving precise control over defect engineering have emerged as critical research priorities. Although conventional characterization techniques face inherent limitations in directly resolving the microstructures of point defects, electron paramagnetic resonance (EPR) spectroscopy has proven to be a pivotal analytical tool for the non-destructive characterization of paramagnetic defects, driving significant advancements in $LiNbO_3$ defect research. This article summarizes the intrinsic and impurity defects that significantly affect the optoelectronic properties of $LiNbO_3$ crystals. Firstly, it elucidates the primary types of point defects, their microstructural characteristics, and their impacts on material properties. Subsequently, it highlights the advancements in EPR technology for studying point defects and provides an in-depth analysis of its advantages in defect analysis. Finally, it proposes the future concerns of studying point defects in $LiNbO_3$ crystals using EPR technology.

1. Introduction

Lithium niobate ($LiNbO_3$) crystals, as a multifunctional crystal material,[1] exhibit the piezoelectric effect, electro-optic effect, nonlinear effect, photorefractive effect, photo-elastic effect, and acousto-optic effect[2] (Fig. 1). Various bulk and thin film devices based on $LiNbO_3$ crystals are widely used in fields such as optical frequency combs,[3,4] optical communication, integrated optics,[5] and lasers.[6] Owing to its excellent optical-electrical properties, $LiNbO_3$ is regarded as "optical silicon" in the optics field. Due to the significant advantages of single-crystal thin-film $LiNbO_3$ in integrated optics, Professor Burrows at Harvard University proposed "Now entering, Lithium Niobate Valley".

Single-crystal defects can be classified into four categories[7] based on their spatial dimensions: point defects, line defects, planar defects, and bulk defects. In $LiNbO_3$ crystals, the main types of defects include bulk defects (*e.g.*, inclusions), planar
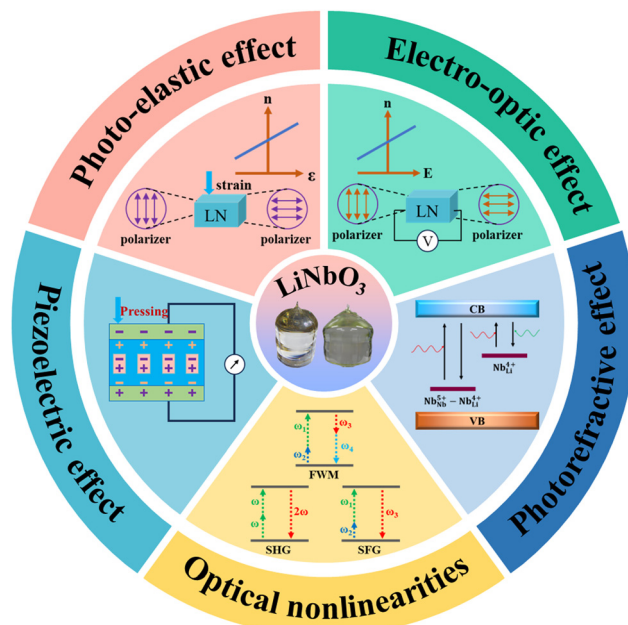
[a] State Key Laboratory of Crystal Materials and Institute of Crystal Materials, Shandong University, 27 Shandanan Road, Jinan 250100, China. E-mail: sangyh@sdu.edu.cn

[b] Jinan Institute of Quantum Technology and Hefei National Laboratory Jinan Branch, Jinan 250101, China. E-mail: wangfl24@163.com, wangdongzhou@jiqt.org

Fig. 1 Properties of $LiNbO_3$ crystals.

defects[8] (twinning boundaries), line defects[9] (dislocations), and point defects[10] (vacancies). Notably, advancements in crystal growth techniques coupled with improved microscopic characterization methodologies have enabled substantial progress in elucidating the formation mechanisms of the first three defect categories, along with effective suppression of their occurrence density. Nevertheless, atomic-scale characterization limitations persist in obscuring the generation dynamics and microstructure of point defects, becoming a critical bottleneck in optimizing the functional performance of LiNbO$_3$ crystals. As is well known, the performance of LiNbO$_3$ crystals is closely related to point defects. However, the formation mechanisms and elimination methods of point defects in LiNbO$_3$ crystals have been scarcely researched.

The investigation of point defects requires the integration of multi-scale characterization techniques, primarily encompassing magnetic resonance spectroscopy (e.g., electron paramagnetic resonance[11] and nuclear magnetic resonance[12]), spectral analysis (photoluminescence[13] and X-ray absorption fine structure[14]), atomic-level microscopy techniques (scanning transmission electron microscopy[15,16]), synchrotron radiation characterization, and computational simulations (density functional theory[17]). Among these, electron paramagnetic resonance (EPR) spectroscopy enables non-destructive acquisition of critical defect information, including local symmetry, coordination environment and charge state through the detection of spin resonance signals from unpaired electrons.[18] This technique is widely recognized as the central methodology for establishing comprehensive point defect models in materials science.[19] Although significant experimental efforts have been devoted to analyzing the point defects in LiNbO$_3$ crystals by EPR spectroscopy, systematic reviews about point defect characterization in LiNbO$_3$ crystals remain strikingly limited. Notably, existing review articles[20,21] predominantly focus on the electronic structure and localized environmental analysis of extrinsic defects, while systematic investigation of the EPR spectrum signatures and defect dynamics in intrinsic defect systems remains notably scarce.

Firstly, this review reviews the pivotal advancements facilitated by EPR spectroscopy in characterizing point defects within LiNbO$_3$ crystals, systematically describing the analysis results of EPR spectroscopy for intrinsic and external defects. Secondly, we also noticed that EPR spectroscopy has more important analytical application in stoichiometric lithium niobate (SLN) crystals. Lastly, the future application of EPR spectroscopy in defects analysis is proposed.

2. Point defects in LiNbO$_3$

The ideal crystal structure of an LiNbO$_3$ crystal consists of oxygen octahedra stacked in coplanar arrangements, with their shared planes perpendicular to the trigonal symmetry axis (i.e., polar axis). These different stacked units interconnect through edge-sharing coordination, forming an oxygen-octahedral framework[22,23] (Fig. 2a). As a ferroelectric material with a Curie temperature of approximately 1483 K (1210 °C), it exhibits distinct paraelectric and ferroelectric phase structures. Its ferroelectric phase structure arises from the cooperative displacement of Li$^+$ ions and Nb^{5+} ions along the crystallographic c-axis, generating spontaneous polarization through ionic rearrangement (Fig. 2b). At this point, cations in the +c direction fill the oxygen octahedron in the form of "–Li Nb–□–Li Nb–□–", where "□" represents vacancies.[22] This structure would be one of the key factors causing LiNbO$_3$ crystals to be plagued by defects.

2.1. Intrinsic defects

LiNbO$_3$ crystal is a typical non-stoichiometric crystal, and its high-quality single crystal is usually grown from a congruent melt (Li : Nb = 48.6 : 51.4) using the Czochralski method, which is called a congruent lithium niobate (CLN) crystal. Due to the absence of Li$^+$, intrinsic defects mainly consisting of Li vacancy (V$_{Li}$) and anti-site Nb (Nb$_{Li}$) appear in the lattice. The existence of these intrinsic defects significantly affects the electro-optical
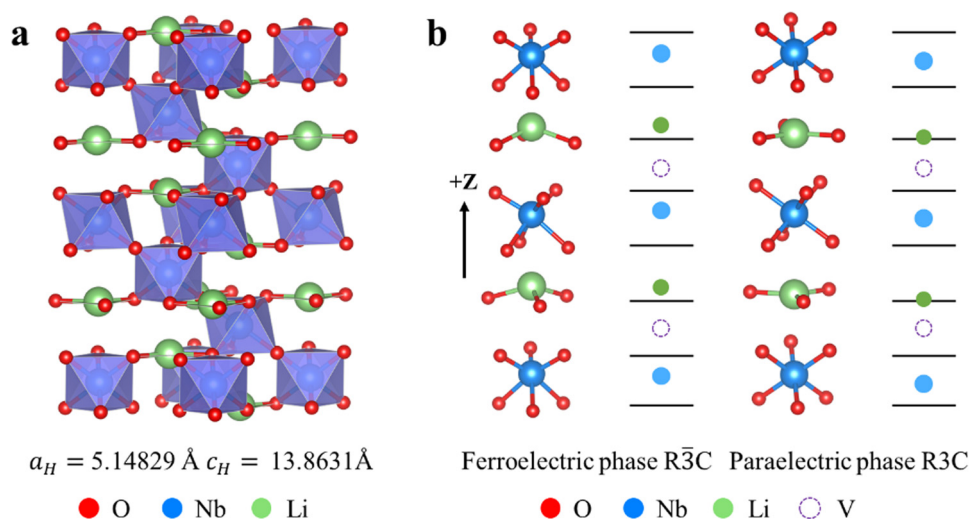

Fig. 2 (a) Ideal structure of LiNbO$_3$, (b) ferroelectric phase (left) and paraelectric phase (right) structure of LiNbO$_3$.

$a_H = 5.14829$ Å $c_H = 13.8631$ Å

Ferroelectric phase R$\bar{3}$C   Paraelectric phase R3C

● O   ● Nb   ● Li

● O   ● Nb   ● Li   ○ V

and nonlinear optical properties of the crystal, thereby limiting their applications in optoelectronic modulators, surface acoustic wave devices, and related fields. Therefore, the regulation of these intrinsic defects and their effects on material performance remains a critical research focus in the field of LiNbO$_3$ crystals.

Over the past few decades, substantial research efforts have been devoted to developing intrinsic defect structure models in LiNbO$_3$ crystals. However, due to inherent theoretical limitations and inconsistencies among various defect models, many have been subsequently abandoned. This chapter focuses on four representative defect models that have demonstrated particular significance in understanding the structural properties of LiNbO$_3$ crystals.

Fay *et al.* (1968) first proposed the oxygen vacancy model,[24] postulating that the absence of Li in crystals generates Li vacancies, while requiring the concomitant formation of oxygen vacancies to maintain charge neutrality. The structural formula of this model is $[Li_{1-2x}V_{2x}]Nb[O_{3-x}V_x]$, where V represents a vacancy. Based on this model, a positive correlation between crystal density and Li content would be expected. However, precise experimental results demonstrate that the crystal density decreases with an increase in Li/Nb ratio.[25] This discrepancy between theoretical predictions and experimental observations ultimately led to the rejection of the oxygen vacancy model.

The Nb vacancy model was proposed,[26] wherein excess Nb occupies octahedral vacancies lacking lithium, forming Nb$_{Li}$, with charge compensation achieved by niobium vacancies (V$_{Nb}$) (Fig. 3a). At this time, the crystal chemical structure formula is $[Li_{1-5x}Nb_{5x}]Nb[O_{1-4x}V_{4x}]O_3$. However, based on the niobium vacancy model, it was calculated that there are 5.9 mol% Nb$_{Li}$ and 4.7 mol% V$_{Nb}$ in the CLN crystal with Li/Nb = 0.942. From an energy perspective, these high concentrations of high valence Nb$_{Li}$ is unstable. Therefore, the ilmenite structure formed by the partial exchange of Li$^+$ and Nb^{5+} was proposed (Fig. 3b). This localized ilmenite structure can transform high-charged Nb$_{Li}^{4+}$ and V$_{Nb}^{5-}$ into simple V$_{Li}^-$, thereby significantly improving the overall energy stability of defect structures based on the niobium vacancy model.

Based on the differences in density and cell parameters of LiNbO$_3$ crystals with different Li/Nb ratios, the Li vacancy model was proposed in 1968. This model suggests that excess Nb in CLN crystals occupies the Li sites to form Nb$_{Li}$, with charge compensation achieved through the formation of Li vacancies (V$_{Li}$), as illustrated in Fig. 3c. The structural formula is $[Li_{1-5x}V_{4x}Nb_x]NbO_3$. Both the lithium vacancy model and niobium vacancy model fundamentally exclude oxygen vacancies in the LiNbO$_3$ crystal, instead proposing the presence of Nb$_{Li}$ defects. The concentration of Nb$_{Li}$ in the lithium vacancy model is only around 1/5 of that in the niobium vacancy model, resulting in a more energetically favorable and stable defect configuration. In 1992, Iyi[27] measured the lattice parameters, density, and crystal powder diffraction data of LiNbO$_3$ crystals with different compositions, supporting the lithium vacancy model. Subsequent experimental studies[28–30] have consistently demonstrated that the lithium vacancy model is a more accurate defect structure model, which has gained widespread acceptance in the scientific community. Density functional theory is commonly used to determine the main intrinsic defects in crystals. According to the formation energy of different defect structures ($E_{V_{Li}} \sim -0.23$ eV, $E_{V_{Nb}} \sim -1.20$ eV, $E_{Nb_{Li}+4V_{Li}} \sim -0.25$ eV, $E_{5Nb_{Li}+4V_{Nb}} \sim -1.12$ eV), Xu *et al.* predicted that the defect cluster composed of four lithium vacancies compensating for anti-site niobium in CLN crystals is the most stable structure.[31] Li *et al.* used a mixed hybrid exchange–correlation functional to improve the computational accuracy and obtained similar conclusions that for most LN crystals, their Fermi level is located in the lower half of the electronic bandgap, and anti-site niobium and Li vacancies coexist (*i.e.* Nb$_{Li}^{...}$ + 4V$_{Li}'$). Nb vacancies may only form under specific conditions.[32]

Table 1 presents a comprehensive comparison of the four major defect models for the LiNbO$_3$ crystal. Among them, the Nb$_{Li}$ defect has emerged as the most widely accepted defect in LiNbO$_3$ crystals, which means that analyses focusing on Nb$_{Li}$ would be the key for defect analysis. Recent studies have further revealed that Nb$_{Li}$ defects exert a significant influence on the physical properties of LiNbO$_3$ crystals, demonstrating predominantly detrimental effects across various crucial material
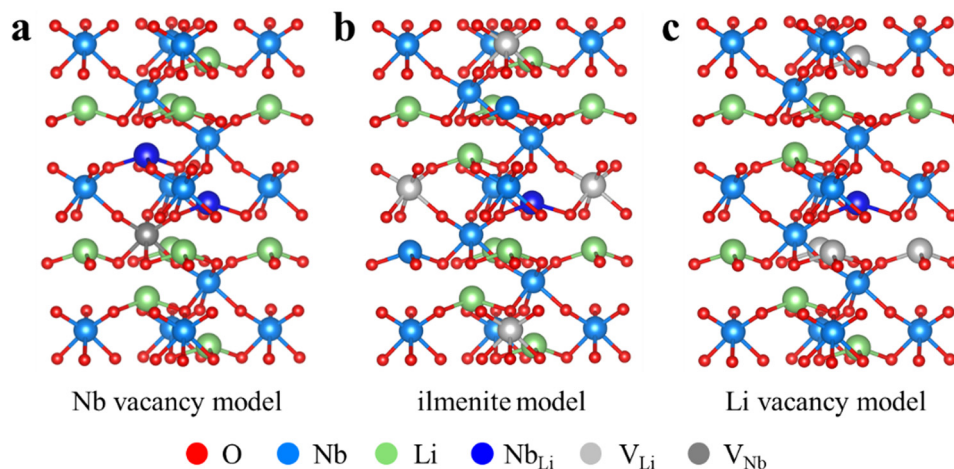

Fig. 3 Defect models in LiNbO$_3$ crystals. (a) Nb vacancy model, (b) ilmenite model, and (c) Li vacancy model.

Table 1 Comparison of defect models for $LiNbO_3$

Model	O vacancy model	Nb vacancy model	Ilmenite model	Li vacancy model
Li vacancy	√	—	—	√
O vacancy	√	—	—	√
Nb vacancy	—	√	√	—
Anti-site Nb	—	√	√	√

characteristics. For example, Nb_{Li} defects act as photorefraction centers[33] between energy levels (Fig. 4a), greatly reducing the optical-damage resistance threshold of the crystal. The electro-optic coefficient, γ_{61}, of the $LiNbO_3$ crystal decreases with a decrease in Li content from a stoichiometric ratio to the congruent component, which was also assigned to the increase in Nb_{Li} defects[34] (Fig. 4b). Furthermore, the pinning effect of Nb_{Li} defects hinders domain inversion,[35] substantially increasing the domain inversion voltage in CLN crystals compared to near stoichiometry lithium niobate (NSLN) crystals (Fig. 4c). In addition, Wang et al. confirmed that the piezoelectric coefficient, d'_{15}, and electromechanical coupling coefficient, k'_{15}, of NLSN crystals are superior to that of CLN crystals at operating temperatures in the range of 0–650 °C, which is also attributed to the contents of Nb_{Li} defects[36] (Fig. 4d).

2.2. Extrinsic defects

The incorporation of various doping elements significantly enriches the properties and broadens the application prospects

of $LiNbO_3$ crystals[40–46] (Fig. 5). For instance, hydrogen atoms typically exist in oxide crystals as OH ions,[47,48] and the presence of unexpected H ions can alter the refractive index of $LiNbO_3$ crystals. Elements such as Mg,[49–51] Zn,[52] In,[53,54] Sc,[55] Sn,[56] Hf[57,58] and Zr,[39,59,60] which possess stable valence states and optical inertness, are employed to enhance the optical damage resistance in $LiNbO_3$ crystals. Conversely, Cu,[61–63] Mn,[64] Fe,[65,66] Ni and Ce[67,68] were used to enhance the photorefractive effect by introducing the impurity defect energy levels in the crystal bandgap. Additionally, rare earth ions such as Er,[69–71] Nd,[72,73] Yb,[46,74] Tb,[75] Dy,[76] Ho[77,78] and Tm[79] serve as active ions, imparting laser properties to $LiNbO_3$.

However, doping engineering also introduced external defects due to the different radii and ionic valence of the dopants. When the doping concentration of Mg exceeds 6 mol%, the optical damage resistance threshold of the Mg:CLN crystal significantly decreases, which is caused by the Mg_{Nb} defect formed by Mg occupying the Nb sites. Lanthanide elements such as Nd and Yb have large ionic radii, which cause severe lattice distortion in $LiNbO_3$ crystals, making them prone to cracking during the growth process. In addition, the segregation effect causes a concentration gradient of doping elements along the crystal axis, which changes the thermal expansion coefficient of the crystal and may lead to cracking during cooling. Obviously, micro defects serve as critical determinants governing the physical properties of $LiNbO_3$ crystals. Consequently, the application of advanced characterization techniques is essential to systematically investigate the formation
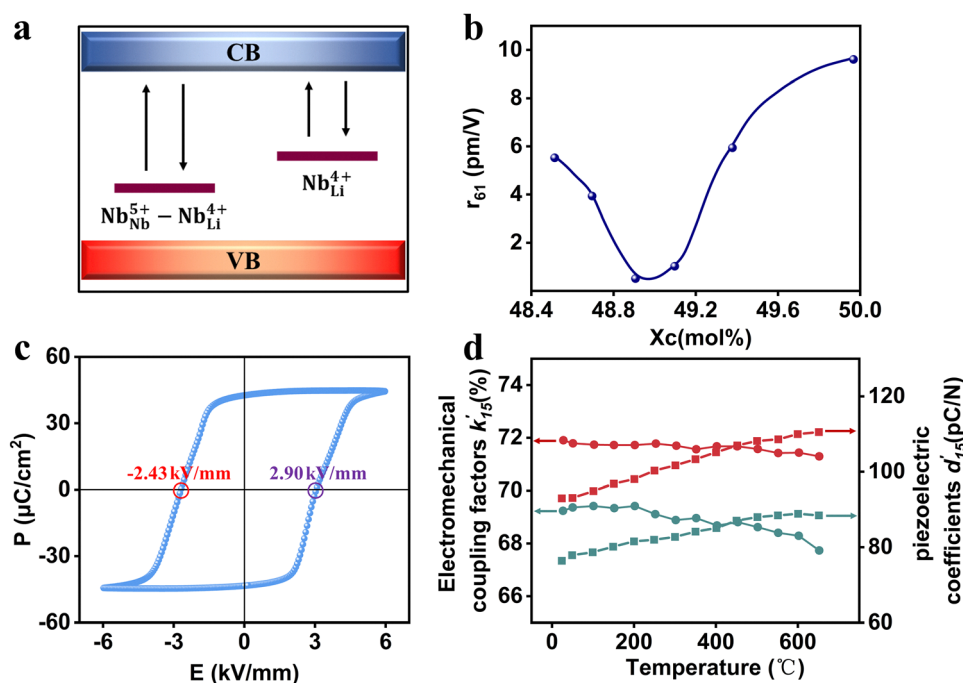

Fig. 4 (a) Nb_{Li} acts as a photorefractive center in CLN crystals. (b) Dependence of the electro-optic coefficient, γ_{61}, on the crystal composition in pure $LiNbO_3$ crystals, where X_c represents the Li content in the $LiNbO_3$ crystal.[34] Reproduced from ref. 34 with permission from AIP Publishing, copyright 1998. (c) Ferroelectric hysteresis loop of NSLN measured at room temperature.[37] Reproduced from ref. 37 with permission from Elsevier, copyright 2022. (d) Variations in electromechanical coupling factors and piezoelectric coefficients as a function of temperature for NSLN (red) and CLN (green) crystals.[36] Reproduced from ref. 36 with permission from the American Chemical Society, copyright 2024.
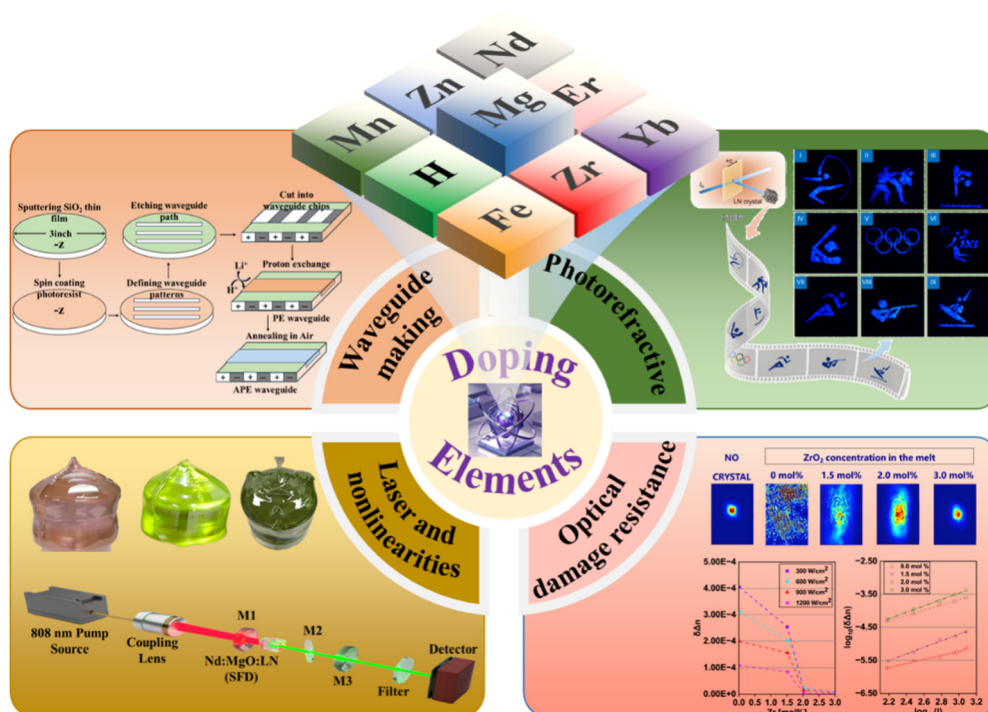
Fig. 5 Application of dopants in the LiNbO₃ crystal.[38,39] Reproduced from ref. 38 with permission from the Editorial Office of Opto-Electronic Journals Group, Institute of Optics and Electronics, copyright 2022. Reproduced from ref. 39 with permission from the Optical Society of America, copyright 2011.

mechanism of defects and their influence on the physical properties of crystals.

Lithium niobate on insulator (LNOI) is completely changing the lithium niobate industry, with advantages such as higher performance and new equipment and applications.[80,81] It not only maintains the excellent optical properties of bulk crystals, but also enables photonic devices/circuits to be easily scaled down to the sub-micron scale.[82] However, processing methods such as ion implantation, ion beam etching, and ion irradiation can cause lattice damage and introduce new defects.[83] Current research on LNOI primarily focuses on fabrication quality, with the use of high-resolution X-ray diffraction to verify the ordering of single crystals[84] and Raman spectroscopy to evaluate the quality of lattice arrangement.[85] There are few reports on the analysis of defects in LNOI, and aberration corrected electron microscopy can be used to directly observe the atomic occupancy. However, EPR technology has not yet been applied to the analysis of defects in LNOI. The defects or damages have a significant impact on the various physical properties of LN crystals. Post-annealing treatment is an effective method for restoring these damages and defects. Usually, H ion implantation into waveguides requires annealing at a temperature of 200–300 °C to reduce optical absorption and improve the waveguide performance. Ashley *et al.*[86] injected a high dose of Ti into LN to form a planar waveguide, and the ion-implanted region was completely amorphized. After annealing at 1000 °C for 1 h, its electro-optic coefficient, γ_{33}, was measured to be 29 pm V^{-1}, which is close to that of bulk crystals. High-temperature annealing helps to restore the electro-optic properties of ion-sliced LN films.[87,88] Moreover, SHG experiments

showed the recovery of the nonlinear coefficient of a LN thin film after annealing at 600 °C.[89]

3. Application of EPR in defect characterization

3.1. Introduction of EPR spectroscopy

EPR spectroscopy is sensitive high-resolution spectrum technology for the detection of unpaired spins, which has been widely used in fields such as physics, chemistry, biology, and materials. Briefly, when EPR spectroscopy is used to study unpaired electron spins in solid materials, Hamiltonian parameters can be used to describe various possible interactions, which generally take the following form:

$$H_{\text{spin}} = H_{\text{EZ}} + H_{\text{HF}} + H_{\text{CF}} + H_{\text{Q}} + H_{\text{NZ}}$$

where H_{EZ} is the electronic Zeeman interaction, representing the interaction between the effective spin, S, and the applied magnetic field, B. As long as there are unpaired electrons, there must be electron Zeeman interactions, which are an essential component of the Hamiltonian parameter. H_{EZ} can be represented by a g-tensor, which can reflect the local point symmetry of defects. H_{HF} is a hyperfine interaction, representing the interaction between the magnetic moment of unpaired electrons and the magnetic moment, I, of nearby atomic nuclei. When $I > 0$, hyperfine splitting occurs, dividing the spectral lines into $(2I + 1)$ lines. Obtaining an effective spin, S, and magnetic moment, I, through EPR spectrum analysis can help us quickly determine the types and charge states of impurity

elements. Due to the influence of the electrical crystal field, additional interactions called fine structure interactions (H_{CF}) can occur in paramagnetic defects with $S > 1/2$, which will result in 2S splitting of the EPR spectrum lines. H_Q and H_{NZ} are the nuclear quadrupole interaction and nuclear Zeeman interaction, respectively, which are small compared to the Zeeman energy and not stated here. For more details, readers can refer to textbooks on EPR spectroscopy, as well as the recent article by Rudowicz,[90] in which the current situation in this area is reviewed and discussed.

3.2. Application of EPR spectroscopy in defect analysis of $LiNbO_3$

The formation of defect structures in crystals is fundamentally governed by the charge states of impurity ions occupying lattice sites and their corresponding charge compensation mechanisms. Excessive Nb occupies the Li sites in CLN crystals to form Nb_{Li} defects, whose concentration and structure have not yet been determined. Due to the complexity of the CLN crystal structure and the limitation of experimental equipment resolution, it is usually difficult to directly observe the structural information of Nb_{Li} defects. Furthermore, the substitution mechanisms of doping elements in CLN crystals, particularly concerning site occupancy preferences and charge compensation, remain poorly understood and require further systematic investigation.

Fortunately, these defects in the crystal are originally paramagnetic or after specific treatment, which can be detected by EPR spectroscopy very accurately. EPR spectroscopy exhibits exceptional sensitivity, and different elements with determined nuclear spin numbers and abundances produce characteristic spectral splitting patterns, which can serve as a "fingerprint" for identifying defect identities.[20] Additionally, ENDOR spectroscopy can probe the surrounding environment of defects, providing crucial insights into their charge compensation mechanisms. Therefore, some progress has been made by EPR and ENDOR technology in analyzing defects in $LiNbO_3$ crystals over the past few decades.

3.2.1. EPR spectrum analysis of intrinsic defect. In $LiNbO_3$ crystals, the Nb_{Li} defect has been widely recognized as the most critical intrinsic defect. It was believed that due to the lower content of Li in the CLN crystal, the higher strength of Nb–O bonds compared to Li–O bonds, the small difference in ionic radius between Li^+ ($r = 0.76$ Å) and Nb^{5+} ($r = 0.69$ Å) and their similar spatial environment, Nb tends to occupy the Li sites to form Nb_{Li}.[10] Peterson discovered two types of lattice environments for Nb^{5+} in the CLN crystal lattice through ^{93}Nb nuclear magnetic resonance experiments, which implied the existence of Nb_{Li}.[26] Therefore, extensive research has been conducted using EPR spectroscopy to analyze the structural information of Nb_{Li}.

Schinner[91] firstly obtained a nearly equidistant 10-line EPR spectrum in CLN crystals after laser irradiation (Fig. 6a). This was attributed to the hyperfine interaction between unpaired electrons and ^{93}Nb nuclei ($I = 9/2$). The relevant Hamiltonian parameters were calculated to be $g_\parallel = 1.90$, $g_\perp = 1.72$, $A_\parallel = 0.011$ cm^{-1} and $A_\perp = 0.023$ cm^{-1}. Its hyperfine splitting and

g-shift are typical features of Nb^{4+} in a distorted oxygen octahedral environment.[92,93] Based on the axial symmetry of the spectrum, they attributed this signal for the first time to the electron self-trapping of the Nb lattice, i.e. $Nb_{Nb}^{5+} + e^- \rightarrow Nb_{Nb}^{4+}$. However, Müller et al. proposed an alternative interpretation by analyzing the angular dependence of the Nb^{4+} signals. Their fitting of the anisotropic g-tensor and A-tensor (Fig. 6b) suggested a reduction in local symmetry around the Nb^{4+} center.[94] The observed symmetry reduction arises from the formation of a charge compensation structure induced by the excess positive charge of Nb_{Li}. This distortion of the local coordination environment provides compelling evidence that the EPR signals originate from the Nb ions occupying the Li sites. Faust[95] noticed that the intensity of EPR spectrum of Nb_{Nb}^{4+} is lower in thermally reduced CLN crystals doped with 6 mol% MgO (Fig. 6c). The reason for this may be that high concentration Mg doping eliminates the Nb_{Li} defects in CLN crystals, resulting in the disappearance of the EPR spectrum belonging to Nb_{Li}^{4+}. Zheng et al.[96] provided the calculated Hamiltonian parameters for Nb_{Li} defects, demonstrating excellent agreement with experimental data. Their analysis further revealed the structural configuration of the defect center, showing that Nb_{Li} is displaced from the ideal Li site by $\Delta z \approx 0.19$ Å along the polar axis, while the coordinating oxygen ions in the plane between Nb_{Li}^{4+} and Nb_{Nb}^{5+} exhibit a lateral displacement of $\Delta x \approx 0.30$ Å away from the C_3 axis. The reason for the offset is that when Nb_{Li}^{5+} captures electrons to form Nb_{Li}^{4+}, the decrease in electrostatic repulsion causes Nb_{Li}^{4+} to shift towards the center of the oxygen octahedron. Meanwhile, due to the overlap of electron clouds, the oxygen ions between Nb_{Li}^{4+} and Nb_{Nb}^{5+} are far away from the oxygen triangle center. Regrettably, the underlying mechanisms responsible for the enhanced Nb_{Li}^{4+} signal in annealed CLN crystals following Xe lamp irradiation remain unclear. In particular, the local charge compensation structure associated with Nb_{Li} defects has not been fully elucidated.

$LiNbO_3$ crystals exhibit darkening when heated to 500 °C under a vacuum, hydrogen, or argon atmosphere, with progressively intensified coloration as the temperature increases.[97] UV-vis absorption spectroscopy shows that annealed samples generate a broad absorption band centered at approximately 500 nm, which shifts to 760 nm after xenon lamp irradiation (optical bleaching).[98,99] The proposed mechanism[98,100] is that the oxygen vacancy introduced during reduction initially traps two electrons to form neutral F-centers, which are responsible for the 500 nm absorption peak. Upon optical bleaching, the F-centers release one electron to become F$^+$-centers. The unpaired electron in the F$^+$-centers interacts through hyperfine coupling with adjacent Nb ions neighboring the oxygen vacancy, manifesting as a 10-line EPR spectrum. Although other intrinsic defects such as lithium and niobium vacancies may exist, they have not yet been experimentally confirmed through spectroscopic characterization.

3.2.2. EPR spectrum analysis of extrinsic defects. The deliberate introduction of extrinsic defects by dopants during crystal growth serves as a crucial strategy for tailoring the properties of materials. Thus, to elucidate the impact of doping elements on the physical properties of crystalline materials, a
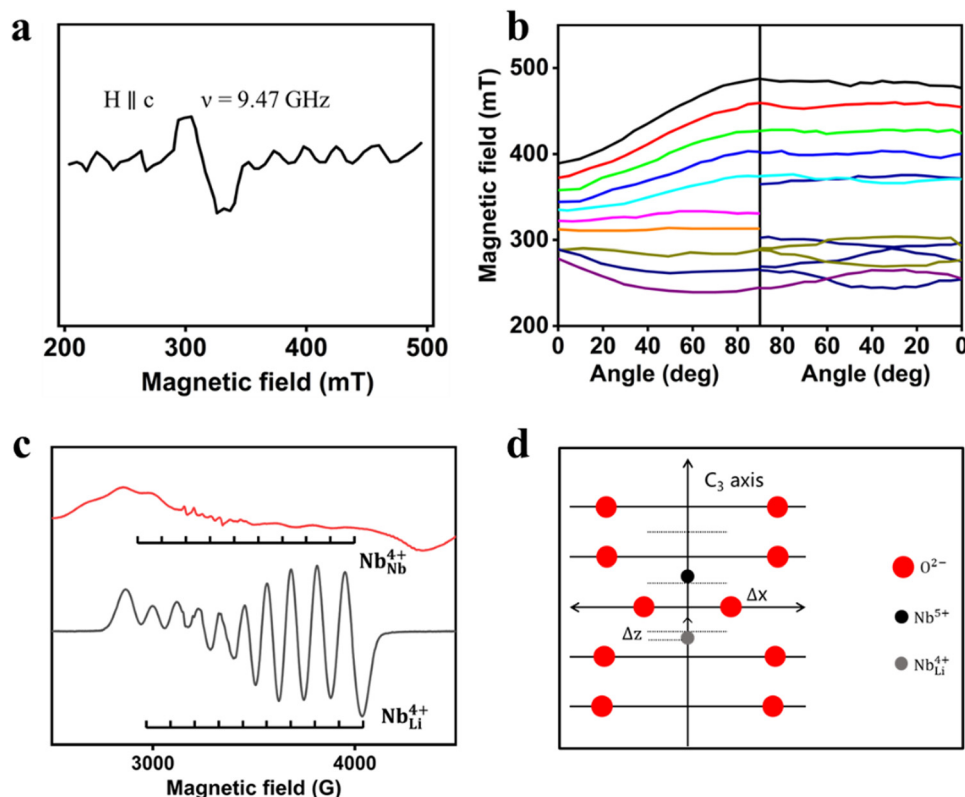
Fig. 6 (a) Two-photon-induced ESR at higher microwave power.[91] Reproduced from ref. 91 with permission from AIP Publishing, copyright 1978. (b) Angular dependence of experimental resonance fields with fitted positions for metastable Nb^{4+}, $T \approx 20$ K, $v \approx 9$ GHz.[94] Reproduced from ref. 94 with permission from Taylor & Francis, copyright 2011. (c) EPR spectrum of Nb^{4+}-type centers in undoped (black) and 6 mol% Mg-doped (red) congruent $LiNbO_3$ crystals after vacuum reduction for the magnetic field parallel to the crystal c axis. (d) Defect structure of Nb_{Li}^{4+} center in $LiNbO_3$.[96] Reproduced from ref. 96 with permission from Elsevier, copyright 2008.

comprehensive understanding of their lattice occupancy behavior and chemical states is essential. The paramagnetic nature of most dopant species in the $LiNbO_3$ crystal makes EPR spectroscopy particularly advantageous for analyzing these extrinsic defects. Among the various dopants, transition metal ions and rare earth ions represent the primary extrinsic species in $LiNbO_3$ crystals, consequently receiving the most extensive attention in EPR-based defect studies.

(1) Transition metal ions

Transition metal ions are widely used to enhance the photorefractive ability of $LiNbO_3$ crystals. Because their unstable valence states can form defect energy levels in the energy band of $LiNbO_3$ crystals, they serve as photorefractive centers. The typical transition metal ions used are Fe, Cu, and Mn, with Fe being the most extensively studied due to its superior ability to improve the photorefractive performance.

For example, five different lattice sites of Fe have been identified in $LiNbO_3$ crystals, namely Fe_1, Fe_2, Fe_3, Fe_4, and Fe_5, respectively. The Fe_1 center with C_3 symmetry in Fe-doped CLN crystals has been found, and several studies[103–106] have consistently reported a zero-field splitting (ZFS) parameter of $b_2^0 \approx 0.1680$ cm^{-1} (Fig. 7a). Zhao[107] calculated the ZFS parameters D and a_F of Fe^{3+} at the Li ($D = 0.860$ cm^{-1}, $a_F = 0.03$ cm^{-1}) and Nb ($D = 1.054$ cm^{-1}, $a_F = 0.114$ cm^{-1}) sites in Fe^{3+}: $LiNbO_3$. The ZFS parameters for Fe^{3+} at Nb sites closely

match experimental results[108] ($D = 1.106$ cm^{-1}, $a_F = 0.128$ cm^{-1}), indicating that the impurity ion Fe^{3+} substitutes Nb^{5+}, rather than Li$^+$ in the $LiNbO_3$ lattice.

When the doping concentration of Mg exceeds the threshold, the Fe_2 center[102] emerges in Fe, Mg co-doped CLN crystals (Fig. 7b). The angle dependence of the EPR spectra indicates that this center exhibits low symmetry.[109] Boker[102] proposed that Fe^{3+} preferentially occupies the Nb^{5+} sites, forming stable charge compensation structures ($Mg_{Li}^+ - Fe_{Nb}^{2-}$). The reason for this is that the smaller ZFS parameter D corresponds to the geometric position of Fe^{3+} occupying the Nb sites, making this configuration energetically favorable in heavily doped CLN crystals. The Fe_3 (Fig. 7c) and Fe_5 (Fig. 7e) centers are distinguished in stoichiometric lithium niobate crystals (grown with K_2O as the flux, denoted as SLN-K) doped with 0.45 mol% Mg and 0.01 mol% Fe.[101,110] The Fe_4 center is observed in the SLN-K crystal with 0.001% Fe (Fig. 7d). Due to the smaller crystal field parameter b_2^0, Fe_3, Fe_4, and Fe_5 are attributed to Fe occupying the Nb sites. The variation in EPR spectra for Fe centers at Nb sites is closely linked to the concentration of intrinsic and extrinsic defects in the crystal lattice. In Mg:CLN crystals, their charge compensation structure is completed by $2Mg_{Li}^+ - Fe_{Nb}^{2-}$, while in SLN-K crystals, charge compensation is achieved through protons or additional Li$^+$.

Mn:Fe:LN crystals with deep and shallow energy levels can utilize dual color storage to exhibit non-volatile storage properties.
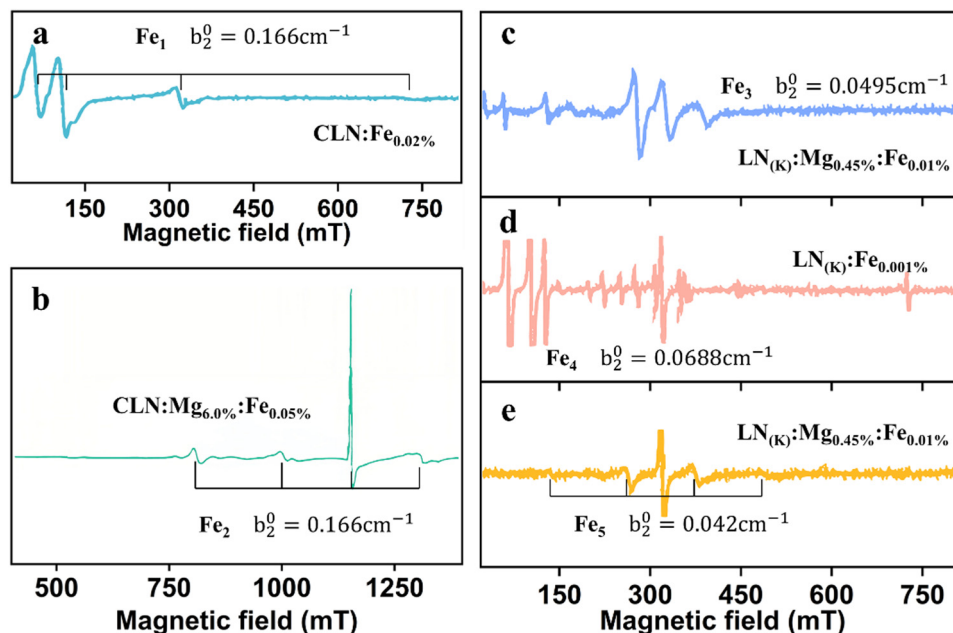
Fig. 7 EPR Fe^{3+} spectra of (a) 0.02% Fe-doped LN crystal.[101] Reproduced from ref. 101 with permission from Taylor & Francis, copyright 2011. (b) 6 mol% Mg, Fe-doped CLN crystal.[102] Reproduced from ref. 102 with permission from IOP Publishing, copyright 1990. (c and e) 0.45% Mg and 0.01% Fe co-doped LN-K crystal.[101] Reproduced from ref. 101 with permission from Taylor & Francis, copyright 2011. (d) 0.001% Fe-doped LN-K crystal.[101] Reproduced from ref. 101 with permission from Taylor & Francis, copyright 2011.

Understanding the substitution mechanism of Mn^{2+} in $LiNbO_3$ crystals is essential for optimizing their performance. The larger hyperfine splitting constant of Mn^{2+} suggests that the Mn–O bond tends to be highly ionic.[111] Peterson[112] proposed that doped ions that do not exhibit a tendency to form covalent bonds, but preferentially substitute at the Li^+ sites. This conclusion is further supported by ENDOR studies,[113] confirming the Li site as the dominant occupancy site for Mn. However, the zero-field splitting parameter b_2^0 of Mn^{2+} decreases with an increase in temperature.[114–116] This trend suggests a reduction in octahedral distortion, consistent with Mn^{2+} shifting toward the center of the $Nb–O_6$ octahedron. This behavior suggests that Mn^{2+} substitutes at the Nb^{5+} site rather than the Li^+ site, contradicting earlier interpretations based on hyperfine splitting and ENDOR studies.

The above-mentioned results indicate that there is still controversy over the occupancy of Mn in $LiNbO_3$ crystals. To resolve this inconsistency, more comprehensive EPR experiments should be designed and performed to unambiguously determine the position of Mn^{2+} in the lattice. Some other transition metal ions, such as Cr^{3+}, Ti^{3+}, Ni^{2+}, and Co^{2+}, in $LiNbO_3$ crystals have also been studied using EPR spectroscopy technology.[117–120]

(2) Rare earth ions

Rare earth (RE) ions are incorporated into $LiNbO_3$ crystals as optically active centers, enabling their widespread use in solid-state lasers,[121] optical amplifiers, and wavelength converters. The spectral properties of these dopants are critically dependent on their local crystal field environment, which is closely related to the site location of the doped ions. RE ions in $LiNbO_3$ crystals can locate at four cation sites, i.e., three octahedral sites (Li^+ site, Nb^{5+} site and a vacant octahedron) or an interstitial

tetrahedral site. However, the actual occupancy situation is much more complex. Spectroscopic studies have shown that even if rare earth ions occupy the same lattice sites in $LiNbO_3$ crystals, they exhibit different spectral properties due to being surrounded by different lattice environments. The lanthanide ions with unpaired electrons located in their 4f orbital are usually used in $LiNbO_3$ crystals. Emission spectroscopy[21] and EPR spectroscopy[122] have identified multiple non-equivalent centers with different symmetries for these ions, suggesting that the actual incorporation mechanism involves a dynamic interplay between dopant ions and the defect structure of the host lattice.

Nd^{3+} defect centers ($g_{\parallel}$ = 1.42 and $g_{\perp}$ = 2.94) with C_3 symmetry in CLN crystals have been found.[125,126] However, the EPR spectrum of Nd^{3+} in CLN crystals displays exceptionally broad lines, making it difficult to resolve contributions from different defect centers or isotopic effects. This explains that why the hyperfine structure was not studied in ref. 110 and 111. The EPR spectrum lines of Nd in NSLN crystals have higher spectral resolution (Fig. 8a). Therefore, eight non-equivalent Nd^{3+} centers were identified in NSLN crystals and the g-tensor values of all the centers were determined. Although all eight centers are the Nd-occupying Li sites,[123] they exhibit different symmetries. Nd_1 and Nd_8 exhibit C_3 symmetry, as evidenced by their angle-independent EPR spectra in the xy-plane (Fig. 8b and c), respectively. The symmetry of the other six defect centers is relatively low, and the reason for the different symmetries is that the defect positions used for charge compensation are different (Table 2).

Earlier studies[126] suggest that the Er^{3+} centers with $g_{\parallel}$ = 15.1–15.4 and $g_{\perp}$ = 2.1 in the CLN crystal have C_3 symmetry (Fig. 9a). However, the angular dependence of the EPR spectrum in the
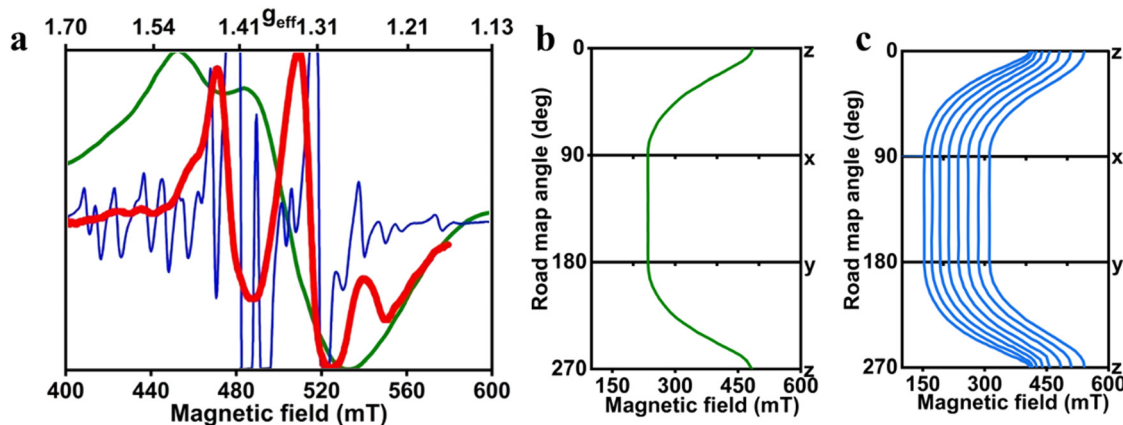
Fig. 8 (a) EPR spectra of Nd^{3+} at B∥z in congruent and nearly stoichiometric $LiNbO_3$ crystals doped with 0.06 wt% Nd_2O_3 in the melt (thick red line: ν = 9.5 GHz and T = 10 K and thin blue line: ν = 9.8 GHz and T = 19 K), as well as in a congruent crystal doped with 1% of Nd (medium green line: X-band, T = 20 K).[123] Reproduced from ref. 123 with permission from AIP Publishing, copyright 2015. (b) Angular dependence of the EPR spectra in nearly stoichiometric LN:Nd^{3+}. T = 19 K, ν = 9.813 GHz.[124] Reproduced from ref. 124 with permission from John Wiley and Sons, copyright 2006. (c) Angular dependence of the EPR spectra in NSLN:Nd^{3+}. T = 19 K, ν = 9.813 GHz.[124] Reproduced from ref. 124 with permission from John Wiley and Sons, copyright 2006.

Table 2 Cartesian components of g-tensors for Nd^{3+} centers in crystallographic axes of $LiNbO_3$.[123] Reproduced from ref. 123 with permission from AIP Publishing, copyright 2015

Center	g_{xx}	g_{yy}	g_{zz}	g_{zy}	$\pm g_{zx}$	$\pm g_{xy}$
Nd_1	2.995	2.995	1.448	0	0	0
Nd_2	3.090	2.920	1.345	−0.040	0.015	0.240
Nd_3	3.277	2.750	1.419	0.024	0.109	0.030
Nd_4	3.430	2.700	1.421	0.035	0.100	0.220
Nd_5	3.43	2.60	1.43	−0.13	0.18	0.20
Nd_6	2.915	3.06	1.454	0.008	0.043	0.025
Nd_7	3.14	3.04	1.488	0.044	0.062	0.030
Nd_8	2.970	2.970	1.563	0	0	0

xy-plane (Fig. 9b) confirms that the Er^{3+} center (g_{xx} = 0.546 ± 0.110, g_{yy} = 1.356 ± 0.024, and g_{zz} = 15.093 ± 0.074) in the CLN crystal has C_1 symmetry.[127–129] The relatively large anisotropy of the g-factor indicates that the Er^{3+} defect center may be located in the distorted Li–O octahedron, i.e. Er^{3+} occupies the Li site. Th. Nolte[130] proposed that this symmetry reduction ($C_3 \rightarrow C_1$) arises from the random distributions of the charge compensation structure Er^{3+}–V_{Li}^-, as illustrated in Fig. 9c. A new Er^{3+} defect center with $g_∥$ = 4.26 ± 0.05 and $g_⊥$ = 7.8 ± 0.1 was identified in Mg, Er:CLN crystals. The mean g value, ($g_∥$ + $2g_⊥$)/3 = 6.6, is characteristic of the Er^{3+} center and closely matches that of the previously reported center.[126] The relatively small g-tensor anisotropy in this case suggests that the Er^{3+} ions are located at the Nb site compare to the previous one.

The tremendous narrowing of EPR spectrum in Yb (0.04 wt%):NSLN crystal (Fig. 10a) compared to Yb:CLN crystal, enabled the resolution of nine non-equivalent Yb^{3+} centers.[132] Among them, the spectral features of the Yb_1, Yb_6, and Yb_9 centers remained invariant under rotation of the magnetic field within the xy-plane, confirming their C_3 symmetry, while the other centers exhibited lower C_1 symmetry. The Yb_1 center with $g_⊥$ = 2.706 ± 0.005 and $g_∥$ = 4.46 ± 0.01 closely resembles the previously reported Yb^{3+} center in CLN crystals.[133] The ENDOR

experimental spectrum[132] (Fig. 10b) reveals the hyperfine interaction between the unpaired electrons of Yb_1 and Nb nuclei, directly indicating that Nb is the nearest neighbor nuclei (Fig. 10c). Therefore, it is reasonable to conclude that Yb_1 is the Yb^{3+} ion substituting for Li^+. Due to the similarity between the characteristics of the Yb_2, Yb_3, Yb_4, Yb_7, and Yb_8 centers (Table 3) and the Yb_1 center, Malovichko[90] proposed that all these defect centers can be attributed to the substitution of Li^+ by Yb^{3+}. This change in symmetry may be caused by the different configurations of Li vacancies around Yb^{3+} or the different positions of Yb^{3+} in the lattice.

4. Summary and prospective

In summary, EPR spectroscopy stands out as a powerful tool for the characterization of defects in $LiNbO_3$ crystals, providing unique insights into the formation and local structure of point defects. Through the comprehensive analysis of EPR spectra and determination of Hamiltonian parameters, this technology enables the precise identification of defect types, quantification of defect concentrations, localization of defect sites, and characterization of structural modifications in the surrounding environment. The structural information derived from Zeeman interactions and zero-field splitting parameters, combined with the analysis of quadrupole interactions and hyperfine couplings between impurity electrons and their host/nuclear environments, provides a robust foundation for structural modeling. These critical insights are crucial to explore the impact of defects on the properties of crystals and how to precisely control defects to improve the performance of crystal devices.

Over recent decades, EPR spectroscopy has undergone remarkable progress in characterizing point defects in $LiNbO_3$ crystals. The evolution of high-sensitivity EPR systems, combined with improved control over crystal stoichiometry and the
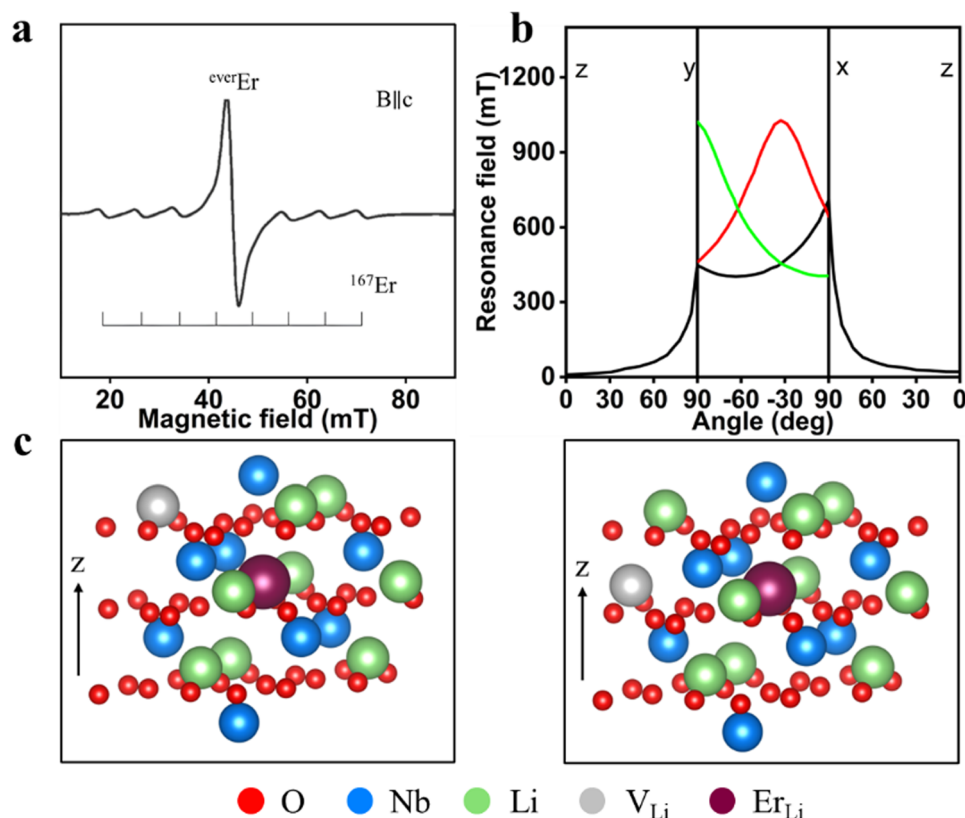
Fig. 9 (a) EPR spectrum of Er^{3+} in $LiNbO_3$, measured at T = 5 K and v_{EPR} = 25 GHz.[130] Reproduced from ref. 130 with permission from Elsevier, copyright 1997. (b) Angular dependence of the EPR spectra of the LN:Er^{3+} crystal measured at 8 K in all three perpendicular planes.[128] Reproduced from ref. 128 with permission from John Wiley and Sons, copyright 2008. (c) Possible models of low-symmetry Er^{3+} centers.[131] Reproduced from ref. 131 with permission from Materials Research Society, copyright 2009.
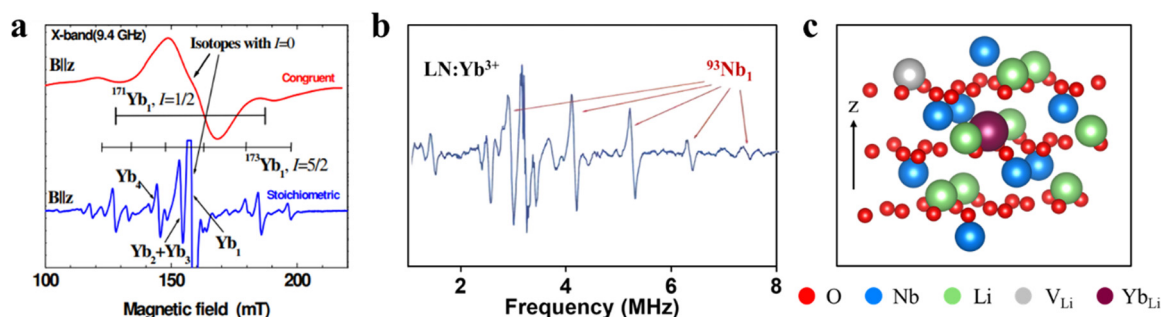

Fig. 10 (a) Assignment of lines of different nonequivalent centers and hyperfine structures of Yb^{3+}.[131] Reproduced from ref. 131 with permission from Materials Research Society, copyright 2009. (b) ENDOR spectrum for the Yb_1 center in SLN:Yb^{3+} at B||z.[132] Reproduced from ref. 132 with permission from John Wiley and Sons, copyright 2008. (c) Model of the Yb_1 center.[132] Reproduced from ref. 132 with permission from John Wiley and Sons, copyright 2008.

integration of advanced characterization tools, is expected to provide unprecedented new insights into defect structures and their interactions with the host lattice. These developments are paving the way for the establishment of more sophisticated defect models, thereby establishing a robust foundation for the growth of high-quality crystals and the fabrication of high-performance devices. Looking ahead, future research may focus on the following aspects.

4.1. Anti-site defects need to be clarified

As the most important intrinsic defects in $LiNbO_3$ crystals, there are still doubts about the concentration, structure, and charge compensation mechanism of Nb_{Li} defects. Although some studies suggest that the 10-line EPR characteristic spectrum produced by xenon lamp irradiation of annealed CLN crystals originate from Nb_{Li}, there is still a lack of direct experimental evidence. Meanwhile, due to the lack of detailed

Table 3 Cartesian components of g-tensors for centers in $LiNbO_3$:Yb^{3+}. The sign $\pm$ reflects the presence of mirror conjugated centers with g_{xy} (L) = $-g_{xy}$ (R), g_{zx} (L) = $-g_{zx}$ (R).[132] Reproduced from ref. 132 with permission from John Wiley and Sons, copyright 2008

Center	g_{xx}	g_{yy}	g_{zz}	g_{zy}	$\pm g_{zx}$	$\pm g_{xy}$
Yb_1	2.706	2.706	4.46	—	—	—
Yb_2	2.84	2.48	4.56	0.22	0.45	0.02
Yb_3	2.63	2.67	4.35	−0.15	0.10	0.17
Yb_4	2.65	2.44	4.56	0.21	0.38	0.08
Yb_6	2.68	2.68	4.44	—	—	—
Yb_7	2.64	2.44	4.56	0.21	0.39	0.024
Yb_8	2.71	2.765	4.36	0.11	0.14	−0.07

information about the anti-site defect structure, it is impossible to construct an appropriate intrinsic defect model; therefore, it is essential to conduct more systematic and in-depth research. Firstly, anti-site Nb exhibits a positive charge state due to charge imbalance and has a stronger attraction to free electrons compared to Nb in the normal lattice position. It is necessary to find a suitable testing temperature that allows electrons at the Nb_{Nb} site to escape, while electrons at the Nb_{Li} site remain bound. At this point, Nb_{Nb}^{5+} exhibits an EPR-silent state, and the characteristic spectrum of Nb^{4+} belongs to Nb_{Li}^{4+}. Secondly, $LiNbO_3$ crystals with different compositions were subjected to the same treatment and their EPR spectra were detected. It can be expected that with an increase in Li/Nb, the characteristic spectral intensity of Nb_{Li}^{4+} decreases and that of Nb_{Nb}^{5+} increases, which will become favorable evidence for the existence of Nb_{Li} defects.

In addition, the thermal stability and dynamic evolution of defects were studied by first-principal theory calculation. However, the theoretical analysis could not draw a clear map of the defect evolution. The thermal activation energy of different defects varies, and at a specific annealing temperature, defects undergo migration-recombination-annihilation, resulting in a decrease in EPR intensity. By drawing the curve of EPR signal intensity and annealing temperature change through an isothermal annealing experiment, different types of point defects can be identified, their migration energy can be measured, and their interactions and evolution paths can be studied.

4.2. In depth analysis of high-resolution EPR spectrum-assisted point defects in NSLN crystals

Although the EPR signals of Nb^{4+} have been detected in CLN crystals, there is currently a lack of sufficient evidence to determine whether the signals originate from Nb_{Li} or Nb_{Nb}. Moreover, there are differences in the Hamiltonian parameters due to spectral broadening and insufficient resolution. When the angle between the microwave direction and the crystallographic c-axis is too large, the intensity of the split signal will decrease, thus being masked by noise. As a result, clear spectral signals can only be observed on the axis. The same problem also arises in the analysis process of doped ion defect centers. It is difficult to comprehensively detect multiple non-equivalent defect centers of doped ions in the crystal and construct suitable defect models. EPR spectrum simulations have indicated that the

linewidth, asymmetry, and intensity of forbidden transitions in the spectrum are closely associated with inherent defects in non-stoichiometric crystals. This is confirmed by the EPR spectrum of SLN-K crystals, which exhibits narrower and more symmetrical features compared to that of CLN crystals.

Moreover, many new EPR signals have been reported in NSLN crystals doped with lanthanide ions. The results are consistent with multiple non-equivalent defect centers shown in the emission spectra, providing theoretical guidance for the occupancy mechanism of doped ions. Doping a small amount of elements in NSLN crystals can significantly improve certain physical properties, such as the improvement of the optical damage resistance of 1 mol% Mg-doped NSLN crystals,[134] which is similar to that of 4.6 mol% Mg-doped CLN crystals. This low concentration doping helps to explore the mechanism of ion doping and achieve precise control of functional crystals. In addition, NSLN crystals may serve as an ideal system for verifying first principles calculations due to their low defect density and perfect lattice structure. Therefore, using EPR spectrum to analyze the defect structure of NSLN crystals has important research value.

4.3. Advancing high-temperature and time-resolved EPR with AI integration

At present, most EPR spectroscopy research is focused on low-temperature conditions, and future research can be devoted to developing high-temperature EPR spectroscopy for defect analysis under conditions closer to practical applications. This technique will help to understand the defect behavior and corresponding physical property changes in materials at high temperatures, providing guidance for the preparation of high-temperature piezo-electric/electro-optic devices using LN crystals. Time-resolved EPR combined with photoexcitation can directly track the carrier trapping dynamics (hole/electron capture rates of defects), photo-induced defect kinetics (formation/annihilation paths of oxygen vacancies under UV irradiation) and spin-dependent charge transfer (inter-defect interactions governing photorefractive response). These results will provide important information for understanding how materials respond to environmental changes in practical applications. These insights are vital for optimizing the carrier lifetimes in electro-optic modulators and suppressing optical damage in high-power lasers. The significant advancement of AI spectroscopy can help researchers process large amounts of complex data more quickly and efficiently, combining machine learning and data science technology to automatically identify and classify defect features using EPR experimental data. This will improve the efficiency and accuracy of data analysis and promote the intelligent development of defect research.

Author contributions

Liu H and Sang Y provided the overall concept for this review and designed the review framework; Qin H wrote the original draft and revised and edited the manuscript; all authors contributed to the general discussion.

Conflicts of interest

There are no conflicts to declare.

Data availability

No primary research results, software or code has been included and no new data were generated or analyzed as part of this review.

Acknowledgements

References

1 H. Liu, Y. Sang, D. Sun, D. Wang and J. Wang, Lithium niobate crystals in the information age: progress and prospects, *J. Synth. Cryst.*, 2021, **50**, 708–715.

2 A. Boes, L. Chang, C. Langrock, M. Yu, M. Zhang, Q. Lin, M. Lončar, M. Fejer, J. Bowers and A. Mitchell, Lithium niobate photonics: Unlocking the electromagnetic spectrum, *Science*, 2023, **379**, eabj4396.

3 Y. He, Q.-F. Yang, J. Ling, R. Luo, H. Liang, M. Li, B. Shen, H. Wang, K. Vahala and Q. Lin, Self-starting bi-chromatic LiNbO$_3$ soliton microcomb, *Optica*, 2019, **6**, 1138–1144.

4 B. Fu, R. Gao, N. Yao, H. Zhang, C. Li, J. Lin, M. Wang, L. Qiao and Y. Cheng, Soliton microcomb generation by cavity polygon modes, *Opto-Electron. Adv.*, 2024, **7**, 240061.

5 M. Wang, Z. Fang, J. Lin, R. Wu, J. Chen, Z. Liu, H. Zhang, L. Qiao and Y. Cheng, Integrated active lithium niobate photonic devices, *Jpn. J. Appl. Phys.*, 2023, **62**, SC0801.

6 D. Sun, Y. Zhang, D. Wang, W. Song, X. Liu, J. Pang, D. Geng, Y. Sang and H. Liu, Microstructure and domain engineering of lithium niobate crystal films for integrated photonic applications, *Light: Sci. Appl.*, 2020, **9**, 197.

7 K. W. Böer and U. W. Pohl, *Semiconductor Physics*, Springer International Publishing, Cham, 2023, pp. 595–648.

8 A. W. Vere, Mechanical twinning and crack nucleation in lithium niobate, *J. Mater. Sci.*, 1968, **3**, 617–621.

9 S. Basu, A. Zhou and M. W. Barsoum, Reversible dislocation motion under contact loading in LiNbO$_3$ single crystal, *J. Mater. Res.*, 2008, **23**, 1334–1338.

10 O. F. Schirmer, O. Thiemann and M. Wöhlecke, Defects in LiNbO$_3$-I. Experimental aspects, *J. Phys. Chem. Solids*, 1992, **52**, 185–200.

11 I. Stefaniuk, Electron paramagnetic resonance study of impurities and point defects in oxide crystals, *Opto-Electron. Rev.*, 2018, **26**, 81–91.

12 A. V. Yatsenko, E. N. Ivanova and N. A. Sergeev, NMR study of intrinsic defects in congruent LiNbO$_3$. 1. "Unoverlapping" defects, *Phys. B*, 1997, **240**, 254–262.

13 T. Kämpfe, A. Haußmann, L. M. Eng, P. Reichenbach, A. Thiessen, T. Woike and R. Steudtner, Time-resolved photoluminescence spectroscopy of Nb$_{Nb}^{4+}$ and O$^-$ polarons in LiNbO$_3$ single crystals, *Phys. Rev. B*, 2016, **93**, 174116.

14 C. Prieto and C. Zaldo, Evidence of the lattice site change of Hf impurity from Hf-doped to Hf:Mg-codoped LiNbO$_3$ single crystals by extended X-ray absorption fine-structure spectroscopy, *J. Phys.: Condens. Matter*, 1994, **6**, L677.

15 J. M. Johnson, S. Im, W. Windl and J. Hwang, Three-dimensional imaging of individual point defects using selective detection angles in annular dark field scanning transmission electron microscopy, *Ultramicroscopy*, 2017, **172**, 17–29.

16 C. Sun, E. Müller, M. Meffert and D. Gerthsen, Analysis of crystal defects by scanning transmission electron microscopy (STEM) in a modern scanning electron microscope, *Adv. Struct. Chem. Imaging*, 2019, **5**, 1.

17 F. Schmidt, A. L. Kozub, U. Gerstmann, W. G. Schmidt and A. Schindlmayr, A density-functional theory study of hole and defect-bound exciton polarons in lithium niobate, *Crystals*, 2022, **12**, 1586.

18 J. Su and J. Du, *Electron paramagnetic resonance spectroscopy: principles and applications*, Science Press, Beijing, 2022.

19 M. A. H. McCausland, Electron paramagnetic resonance: Techniques and applications, *Phys. Bull.*, 1969, **20**, 237.

20 V. G. Grachev and G. I. Malovichko, Structures of impurity defects in lithium niobate and tantalate derived from electron paramagnetic and electron nuclear double resonance data, *Crystals*, 2021, **11**, 339.

21 G. Malovichko, V. Bratus, M. Munro, E. Kokanyan, S. Okulov and V. Grachev, Multifrequency spectroscopy of laser active centers Nd^{3+} and Yb^{3+} in nearly stoichiometric LiNbO$_3$, *Phys. Status Solidi C*, 2007, **4**, 1346–1351.

22 Y. Kong, J. Xu, G. Zhang and S. Liu, *Multi-functional opto-electronic material: lithium niobate crystal*, Science Press, Beijing, 2005.

23 Madhu, M. Jain and P. P. Dwivedi, in *Advances in Materials Processing and Manufacturing Applications*, ed. A. Patnaik, E. Kozeschnik and V. Kukshal, Springer Singapore, Singapore, 2021, pp. 345–352.

24 H. Fay, W. J. Alford and H. M. Dess, Dependence of second-harmonic phase-matching temperature in LiNbO$_3$ crystals on melt composition, *Appl. Phys. Lett.*, 1968, **12**, 89–92.

25 S. C. Abrahams and P. Marsh, Defect structure dependence on composition in lithium niobate, *Acta Crystallogr., Sect. B: Struct. Sci.*, 1986, **42**, 61–68.

26 G. E. Peterson and A. Carnevale, ^{93}Nb NMR linewidths in nonstoichiometric lithium niobate, *J. Chem. Phys.*, 1972, **56**, 4848–4851.

27 N. Iyi, K. Kitamura, F. Izumi, J. K. Yamamoto, T. Hayashi, H. Asano and S. Kimura, Comparative study of defect structures in lithium niobate with different compositions, *J. Solid State Chem.*, 1992, **101**, 340–352.

28 A. P. Wilkinson, A. K. Cheetham and R. H. Jarman, The defect structure of congruently melting lithium niobate, *J. Appl. Phys.*, 1993, **74**, 3080–3083.

29 S. Kojima, Composition variation of optical phonon damping in lithium niobate crystals, *Jpn. J. Appl. Phys.*, 1993, **32**, 4373–4376.

30 J. Blümel, E. Born and T. Metzger, Solid state NMR study supporting the lithium vacancy defect model in congruent lithium niobate, *J. Phys. Chem. Solids*, 1994, **55**, 589–593.

31 H. Xu, D. Lee, J. He, S. B. Sinnott, V. Gopalan, V. Dierolf and S. R. Phillpot, Stability of intrinsic defects and defect clusters in $LiNbO_3$ from density functional theory calculations, *Phys. Rev. B: Condens. Matter Mater. Phys.*, 2008, **78**, 174103.

32 Y. Li, W. G. Schmidt and S. Sanna, Intrinsic $LiNbO_3$ point defects from hybrid density functional calculations, *Phys. Rev. B: Condens. Matter Mater. Phys.*, 2014, **89**, 094111.

33 M. Fontana, K. Chah, M. Aillerie, R. Mouras and P. Bourson, Optical damage resistance in undoped $LiNbO_3$ crystals, *Opt. Mater.*, 2001, **16**, 111–117.

34 F. Abdi, M. Aillerie, P. Bourson, M. D. Fontana and K. Polgar, Electro-optic properties in pure $LiNbO_3$ crystals from the congruent to the stoichiometric composition, *J. Appl. Phys.*, 1998, **84**, 2251–2254.

35 H. Bo, Q. Meng, H. Hu, H. Zhao, Z. Zhang, Q. Zhang and C. Zhang, Temperature-dependent ferroelectric properties of near stoichiometric lithium niobate single crystal, *Appl. Phys. A: Mater. Sci. Process.*, 2018, **124**, 691.

36 G. Wang, F. Wang, L. Xie, D. Wang, W. Song, Y. Sang, H. Liu, X. Zhao and F. Yu, Near stochiometric $LiNbO_3$ crystal: the Piezoelectric features and the shear horizontal guided wave transducer for structural health monitoring up to 650 °C, *ACS Appl. Mater. Interfaces*, 2024, **16**, 47902–47911.

37 F. Wang, D. Sun, Q. Liu, Y. Song, F. Zhang, W. Zhou, Y. Sang, D. Wang and H. Liu, Growth of large size near-stoichiometric lithium niobate single crystals with low coercive field for manufacturing high quality periodically poled lithium niobate, *Opt. Mater.*, 2022, **125**, 112058.

38 S. Wang, Y. Shan, D. Zheng, S. Liu, F. Bo, H. Liu, Y. Kong and J. Xu, The real-time dynamic holographic display of LN:Bi,Mg crystals and defect-related electron mobility, *Opto-Electron. Adv.*, 2022, **5**, 210135.

39 G. Nava, P. Minzioni, W. Yan, J. Parravicini, D. Grando, E. Musso, I. Cristiani, N. Argiolas, M. Bazzan, M. V. Ciampolillo, A. Zaltron, C. Sada and V. Degiorgio, Zirconium-doped lithium niobate: photorefractive and electro-optical properties as a function of dopant concentration, *Opt. Mater. Express*, 2011, **1**, 270.

40 X. Zhang, G. Liang and Z. Xu, Defect structure and holographic storage properties of $LiNbO_3$:Zr:Fe:Cu crystals with various Li/Nb ratios, *Opt. Mater.*, 2019, **96**, 109318.

41 M. N. Palatnikov, A. V. Kadetova, L. A. Aleshina, O. V. Sidorova, N. V. Sidorov, I. V. Biryukova and O. V. Makarova, Growth, structure, physical and chemical characteristics in a series of LiNbO3:Er crystals of different composition grown in one technological cycle, *Opt. Laser Technol.*, 2022, **147**, 107671.

42 K. Kasemir, K. Betzler, B. Matzas, B. Tiegel, T. Wahlbrink, M. Wöhlecke, B. Gather, N. Rubinina and T. Volk, Influence of Zn/In codoping on the optical properties of lithium niobate, *J. Appl. Phys.*, 1998, **84**, 5191–5193.

43 J. G. Marques and K. Lorenz, Lattice location of Hf and its interaction with other impurities in $LiNbO_3$: a review, *Opt. Eng.*, 2014, **53**, 060901.

44 K. Lengyel, L. Kovács, Á. Péter, K. Polgár and G. Corradi, The effect of stoichiometry and Mg doping on the Raman spectra of $LiNbO_3$:Mg crystals, *Appl. Phys. B*, 2007, **87**, 317–322.

45 D. Sun, Y. Leng, Y. Sang, X. Kang, S. Liu, X. Qin, K. Cui, B. K. Wan Hairul Anuar, H. Liu and Y. Bi, $Nd:MgO:LiTaO_3$ crystal for self-doubling laser applications: growth, structure, thermal and laser properties, *CrystEngComm*, 2013, **15**, 7468.

46 F. Wang, X. Kang, L. Liang, W. Song, D. Sun, J. Wang, H. Liu and Y. Sang, Yb sensitized near-stoichiometric $Er:LiNbO_3$ single crystal: A Matrix for optical communication and upconversion emission, *Cryst. Growth Des.*, 2018, **18**, 1495–1500.

47 J. M. Cabrera, Hydrogen defects in $LiNbO_3$ and applications, *Radiat. Eff. Defects Solids*, 1995, **136**, 79–83.

48 J. M. Cabrera, J. Olivares, M. Carrascosa, J. Rams, R. Müller and E. Diéguez, Hydrogen in lithium niobate, *Adv. Phys.*, 1996, **45**, 349–392.

49 J. Wen, L. Wang, Y. Tang and H. Wang, Enhanced resistance to photorefraction and photovoltaic effect in Li-rich $LiNbO_3$:Mg crystals, *Appl. Phys. Lett.*, 1988, **53**, 260–261.

50 J. E. Midwinter, Lithium niobate: Effects of composition on the refractive indices and optical second-harmonic generation, *J. Appl. Phys.*, 1968, **39**, 3033–3038.

51 Y. Kong, B. Li, Y. Chen, Z. Huang, S. Chen, L. Zhang, S. Liu, J. Xu, H. Liu, Y. Wang, W. Yan, X. Xie, X. Li, L. Shi, W. Zhang and G. Zhang, *Photorefractive Effects, Materials, and Devices*, OSA, La Colle sur Loup, 2003, p. 53.

52 T. R. Volk, V. I. Pryalkin and N. M. Rubinina, Optical-damage-resistant $LiNbO_3$:Zn crystal, *Opt. Lett.*, 1990, **15**, 996.

53 Y. Kong, J. Wen and H. Wang, New doped lithium niobate crystal with high resistance to photorefraction—$LiNbO_3$:In, *Appl. Phys. Lett.*, 1995, **66**, 280–281.

54 S. Sulyanov and T. Volk, Lattice parameters of optical damage resistant In-doped $LiNbO_3$ crystals, *Crystals*, 2018, **8**, 210.

55 J. K. Yamamoto, K. Kitamura, N. Iyi, S. Kimura, Y. Furukawa and M. Sato, Increased optical damage resistance in Sc_2O_3-doped $LiNbO_3$, *Appl. Phys. Lett.*, 1992, **61**, 2156–2158.

56 L. Wang, S. Liu, Y. Kong, S. Chen, Z. Huang, L. Wu, R. Rupp and J. Xu, Increased optical-damage resistance in tin-doped lithium niobate, *Opt. Lett.*, 2010, **35**, 883.

57 P. Minzioni, I. Cristiani, J. Yu, J. Parravicini, E. P. Kokanyan and V. Degiorgio, Linear and nonlinear optical properties of Hafnium-doped lithium-niobate crystals, *Opt. Express*, 2007, **15**, 14171.

58 P. Galinetto, F. Rossella, I. Cristiani, P. Minzioni, V. Degiorgio and E. P. Kokanyan, Structural and optical

properties of hafnium-doped lithium-niobate crystals, *Phys. Status Solidi C*, 2007, **4**, 1372–1375.

59 Y. Kong, S. Liu, Y. Zhao, H. Liu, S. Chen and J. Xu, Highly optical damage resistant crystal: zirconium-oxide-doped Lithium Niobate, *Appl. Phys. Lett.*, 2007, **91**, 081908.

60 L. Sun, F. Guo, Q. Lv, H. Yu, H. Li, W. Cai, Y. Xu and L. Zhao, Increased optical damage resistance of Zr:LiNbO$_3$ crystals, *Cryst. Res. Technol.*, 2007, **42**, 1117–1122.

61 K. Buse, F. Jermann and E. Krätzig, *European Materials Research Society Symposia Proceedings*, Elsevier, 1995, vol. 48, pp. 237–240.

62 E. Krätzig and H. Kurz, Photo-induced currents and voltages in LiNbO$_3$, *Ferroelectrics*, 1976, **13**, 295–296.

63 F. Caccavale, C. Sada, F. Segato, L. D. Bogomolova, N. A. Krasil'nikova, Yu. N. Korkishko, V. A. Fedorov and T. V. Morozova, Copper–lithium ion exchange in LiNbO$_3$, *J. Mater. Res.*, 2000, **15**, 1120–1124.

64 Y. Yang, A. Adibi and D. Berben, The role of Mn in photorefractive LiNbO$_3$, *Photorefractive Effects, Materials, and Devices*, 2001, p. 101.

65 E. Krätzig, Photorefractive effects and photoconductivity in LiNbO$_3$:Fe, *Ferroelectrics*, 1978, **21**, 635–636.

66 C. Prieto and C. Zaldo, Determination of the lattice site of Fe in photorefractive LiNbO$_3$, *Solid State Commun.*, 1992, **83**, 819–821.

67 Y. Fan, H. Li and L. Zhao, Structure and optical properties of near stoichiometric Ce:LiNbO$_3$ crystals, *Cryst. Res. Technol.*, 2007, **42**, 493–497.

68 X. Zhen, M. Li, C. Liu and Y. Xu, in *Growth and holographic storage properties of stoichiometric Ce:LiNbO$_3$ crystals*, ed. D. Xu and S. Ogawa, Shanghai, China, 2002, p. 422.

69 E. Lallier, Rare-earth-doped glass and LiNbO$_3$ waveguide lasers and optical amplifiers, *Appl. Opt.*, 1992, **31**, 5276.

70 W. Sohler, *Optical Fiber Communications*, OFC, 1996, pp. 251–253.

71 Y. Qian, Z. Xie, R. Wang, H. Zhang and Q. Wu, Efficient 1.54μm laser property in near- stoichiometric Er:LiNbO3 crystal, *Opt. Laser Technol.*, 2015, **74**, 173–177.

72 Y. Lu, Y. Lu, C. Xue and N. Ming, Growth of Nd^{3+}-doped LiNbO$_3$ optical superlattice crystals and its potential applications in self-frequency doubling, *Appl. Phys. Lett.*, 1996, **68**, 1467–1469.

73 D. Z. Wang, D. H. Sun, X. L. Kang, Y. H. Sang, B. X. Yan, H. Liu and Y. Bi, Periodically poled self-frequency-doubling green laser fabricated from Nd:Mg:LiNbO$_3$ single crystal, *Opt. Express*, 2015, **23**, 17727.

74 J. Capmany, E. Montoya, V. Bermúdez, D. Callejo, E. Diéguez and L. E. Bausá, Self-frequency doubling in Yb^{3+} doped periodically poled LiNbO$_3$:MgO bulk crystal, *Appl. Phys. Lett.*, 2000, **76**, 1374–1376.

75 M. N. Palatnikov, N. V. Sidorov, A. V. Kadetova, N. A. Teplyakova, O. V. Makarova and D. V. Manukovskaya, Concentration threshold in optically nonlinear LiNbO$_3$:Tb crystals, *Opt. Laser Technol.*, 2021, **137**, 106821.

76 G. Dominiak-Dzik, W. Ryba-Romanowski, M. N. Palatnikov, N. V. Sidorov and V. T. Kalinnikov, Dysprosium-doped LiNbO$_3$ crystal. Optical properties and effect of temperature on fluorescence dynamics, *J. Mol. Struct.*, 2004, **704**, 139–144.

77 L. Dai, Z. Yan, S. Jiao, C. Xu and Y. Xu, Effect of [Li]/[Nb] ratios on the absorption and up-conversion emission spectra in In:Yb:Ho:LiNbO$_3$ crystal, *J. Alloys Compd.*, 2015, **644**, 502–505.

78 A. Lorenzo, L. E. Bausa and J. G. Sole, Optical characterization of Ho^{3+} ions in LiNbO$_3$ and in LiNbO$_3$:MgO crystals, *J. Phys.: Condens. Matter*, 1994, **6**, 1065–1078.

79 M. Quintanilla, E. Cantelar, J. A. Sanz-García and F. Cussó, Growth and optical characterization of Tm^{3+}-doped LiNbO$_3$, *Opt. Mater.*, 2008, **30**, 1098–1102.

80 J. Lin, F. Bo, Y. Cheng and J. Xu, Advances in on-chip photonic devices based on lithium niobate on insulator, *Photon. Res.*, 2020, **8**, 1910.

81 S. Saravi, T. Pertsch and F. Setzpfandt, Lithium Niobate on Insulator: An Emerging Platform for Integrated Quantum Photonics, *Adv. Opt. Mater.*, 2021, **9**, 2100789.

82 D. Zhu, L. Shao, M. Yu, R. Cheng, B. Desiatov, C. J. Xin, Y. Hu, J. Holzgrafe, S. Ghosh, A. Shams-Ansari, E. Puma, N. Sinclair, C. Reimer, M. Zhang and M. Lončar, Integrated photonics on thin-film lithium niobate, *Adv. Opt. Photon.*, 2021, **13**, 242.

83 F. Chen, Photonic guiding structures in lithium niobate crystals produced by energetic ion beams, *J. Appl. Phys.*, 2009, **106**, 081101.

84 Q. Li, H. Zhang, H. Zhu and H. Hu, Characterizations of Single-Crystal Lithium Niobate Thin Films, *Crystals*, 2022, **12**, 667.

85 J. You, W. Wu, C. Jin, L. Qu, D. Zhang, J. Qi, W. Cai, M. Ren and J. Xu, Raman characterization of focused ion beam fabricated lithium niobate film, *J. Appl. Phys.*, 2024, **135**, 033101.

86 P. R. Ashley, W. S. C. Chang, C. J. Buchal and D. K. Thomas, Guided wave modulators in Ti ion implanted LiNbO$_3$ waveguides, *J. Light Technol.*, 1989, **7**, 855–862.

87 P. Rabiei and P. Gunter, Optical and electro-optical properties of submicrometer lithium niobate slab waveguides prepared by crystal ion slicing and wafer bonding, *Appl. Phys. Lett.*, 2004, **85**, 4603–4605.

88 T. A. Ramadan, M. Levy and R. M. Osgood, Electro-optic modulation in crystal-ion-sliced z-cut LiNbO$_3$ thin films, *Appl. Phys. Lett.*, 2000, **76**, 1407–1409.

89 A. M. Radojevic, M. Levy, H. Kwak and R. M. Osgood Jr., Strong nonlinear optical response in epitaxial liftoff single-crystal LiNbO$_3$ films, *Appl. Phys. Lett.*, 1999, **75**, 2888–2890.

90 C. Rudowicz, Concept of spin Hamiltonian, forms of zero field splitting and electronic Zeeman Hamiltonians and relations between parameters used in EPR, *Magn. Reson. Rev.*, 1987, **13**, 1–89.

91 O. F. Schirmer and D. V. D. Linde, Two-photon- and x-ray-induced Nb^{4+} and O$^-$ small polarons in LiNbO$_3$, *Appl. Phys. Lett.*, 1978, **33**, 35–38.

92 H. H. Pieper and K. Schwochau, Hyperfine and superhyperfine EPR spectra of Tc(IV) and Re(IV) in tin dioxide single crystals, *J. Chem. Phys.*, 1975, **63**, 4716–4722.

93 B. R. McGarvey, The isotropic hyperfine interaction, *J. Phys. Chem.*, 1967, **71**, 51–66.

94 H. Müller and O. F. Schirmer, Microscopic structure of Nb_{Li} related defects in reduced undoped $LiNbO_3$, *Ferroelectrics*, 1992, **125**, 319–324.

95 B. Faust, H. Müller and O. F. Schirmer, Free small polarons in $LiNbO_3$, *Ferroelectrics*, 1994, **153**, 297–302.

96 W. Zheng, W. Fang, L. He and Y. Mei, Spin Hamiltonian parameters and defect structure for the X-ray-induced Nb_{Li}^{4+} center in $LiNbO_3$ crystal, *J. Alloys Compd.*, 2008, **453**, 32–35.

97 J. L. Ketchum, K. L. Sweeney, L. E. Halliburton and A. F. Armington, Vacuum annealing effects in lithium niobate, *Phys. Lett. A*, 1983, **94**, 450–453.

98 K. L. Sweeney and L. E. Halliburton, Oxygen vacancies in lithium niobate, *Appl. Phys. Lett.*, 1983, **43**, 336–338.

99 L. E. Halliburton, K. L. Sweeney and C. Y. Chen, Electron spin resonance and optical studies of point defects in lithium niobate, *Nucl. Instrum. Methods Phys. Res., Sect. B*, 1984, **1**, 344–347.

100 G. G. DeLeo, J. L. Dobson, M. F. Masters and L. H. Bonjack, Electronic structure of an oxygen vacancy in lithium niobate, *Phys. Rev. B: Condens. Matter Mater. Phys.*, 1988, **37**, 8394–8400.

101 V. Grachev, G. Malovichko and E. Kokanyan, Optimization of lithium niobate for advanced applications by variation of extrinsic and intrinsic defect subsystems, *Ferroelectrics*, 2001, **258**, 131–140.

102 A. Boker, H. Donnerberg, O. F. Schirmer and X. Feng, Two sites of Fe^{3+} in highly Mg-doped $LiNbO_3$, *J. Phys.: Condens. Matter*, 1990, **2**, 6865–6868.

103 D. J. Keeble, M. Loyo-Menoyo, Y. Furukawa and K. Kitamura, Electron paramagnetic resonance of Fe^{3+} in $LiNbO_3$, *Phys. Rev. B: Condens. Matter Mater. Phys.*, 2005, **71**, 224111.

104 H. H. Towner, Y. M. Kim and H. S. Story, EPR studies of crystal field parameters in Fe^{3+}: $LiNbO_3$, *J. Chem. Phys.*, 1972, **56**, 3676–3679.

105 H.-D. Pfannes, A. Putzka and J. F. Sampaio, Electronic structure and spin relaxation of Fe(III) in $LiNbO_3$, *Hyperfine Interact.*, 1986, **28**, 785–788.

106 R. C. Santana, M. C. Terrile, A. C. Hernandes, M. R. B. Andreeta and G. E. Barberis, Electron spin resonance study of Fe^{3+} in $LiNbO_3$ single crystals: Bulk and fibres, *Solid State Commun.*, 1997, **103**, 61–64.

107 M. G. Zhao and M. Chiu, Substitution site of the Fe^{3+} impurity in crystalline $LiNbO_3$, *Phys. Rev. B: Condens. Matter Mater. Phys.*, 1994, **49**, 12556–12558.

108 J. B. Herrington, B. Dischler and J. Schneider, An EPR investigation of Fe^{3+} and Mn^{2+} in $LiNbO_3$, *Solid State Commun.*, 1972, **10**, 509–511.

109 G. I. Malovichko, V. G. Grachov and E. P. Kokanyan, Widths and intensities of ESR lines of iron-group impurities in nonstoichiometric lithium niobate crystals, *Phys. Solid State*, 1986, **28**, 1453–1458.

110 G. I. Malovichko, V. G. Grachev, O. F. Schirmer and B. Faust, New axial Fe^{3+} centres in stoichiometric lithium niobate crystals, *J. Phys.: Condens. Matter*, 1993, **5**, 3971–3976.

111 T. Takeda, A. Watanabe and K. Sugihara, Spacing of the hyperfine sextet in Mn^{2+} ESR in $LiNbO_3$, *Phys. Lett. A*, 1968, **27**, 114–115.

112 E. V. Charnaya, V. T. Gabrielyan, V. S. Kasperovich and S. Klimko, Li^7 NMR in $LiNbO_3$ crystals with different nonstoichiometry, *Ferroelectrics*, 1997, **202**, 115–119.

113 G. Corradi, H. Sothe, J.-M. Spaeth and K. Polgar, Mn^{2+} defects in $LiNbO_3$: an electron nuclear double resonance (ENDOR) investigation of the Mn^{2+} site and the local disorder, *J. Phys.: Condens. Matter*, 1990, **2**, 6603–6618.

114 T. H. Yeom and S. H. Lee, Temperature dependence of Mn^{2+} paramagnetic Ion in a stoichiometric $LiNbO_3$ single crystal, *J. Magn.*, 2013, **18**, 221–224.

115 V. K. Jain, Superposition model analysis of zero-field splitting of Mn^{2+} in $LiNbO_3$, *Solid State Commun.*, 1992, **84**, 669–672.

116 D. G. Rexford and Y. M. Kim, Electron-spin resonance studies of crystal field parameters in Mn^{2+}: $LiNbO_3$, *J. Chem. Phys.*, 1972, **57**, 3094–3098.

117 G. Corradi, H. Sothe, J.-M. Spaeth and K. Polgar, Electron spin resonance and electron-nuclear double-resonance investigation of a new Cr^{3+} defect on an Nb site in $LiNbO_3$:Mg:Cr, *J. Phys.: Condens. Matter*, 1991, **3**, 1901–1908.

118 G. Corradi, I. M. Zaritskii, A. Hofstaetter, K. Polgár and L. G. Rakitina, Ti^{3+} on Nb site: A paramagnetic Jahn-Teller center in vacuum-reduced $LiNbO_3$: Mg: Ti single crystals, *Phys. Rev. B: Condens. Matter Mater. Phys.*, 1998, **58**, 8329–8337.

119 Z. Y. Yang, C. Rudowicz and Y. Y. Yeung, Microscopic spin-Hamiltonian parameters and crystal field energy levels for the low C_3 symmetry Ni^{2+} centre in $LiNbO_3$ crystals, *Phys. B*, 2004, **348**, 151–159.

120 V. G. Grachev, K. Hansen, M. Meyer, E. P. Kokanyan and G. I. Malovichko, Substitution mechanisms and location of Co^{2+} ions in congruent and stoichiometric lithium niobate crystals derived from electron paramagnetic resonance data, *Mater. Res. Express*, 2017, **4**, 036204.

121 Q. Luo, F. Bo, Y. Kong, G. Zhang and J. Xu, Advances in lithium niobate thin-film lasers and amplifiers: a review, *Adv. Photon.*, 2023, **5**, 034002.

122 R. Jablonski, I. Pracka and M. Swirkowicz, *Electron spin resonance spectra of Nd^{3+}, Dy^{3+}, Er^{3+} and Yb^{3+} in $LiNbO_3$*, Zakopane, Poland, 1997.

123 V. Grachev, M. Munro, E. Kokanyan and G. Malovichko, Determination of g-tensors of low-symmetry Nd^{3+} centers in $LiNbO_3$ by rectification of angular dependence of electron paramagnetic resonance spectra, *J. Appl. Phys.*, 2015, **118**, 044103.

124 G. Malovichko, V. Grachev, S. Okulov, E. Kokanyan, F. Henecker, A. Hofstaetter and O. Schirmer, EPR of Nd^{3+} in congruent and nearly stoichiometric lithium niobate, *Phys. Status Solidi B*, 2006, **243**, 409–415.

125 G. Burns, D. F. O'kane and R. S. Title, Optical and Electron-Spin-Resonance Spectra of Yb^{3+}, Nd^{3+}, and Cr^{3+} in $LiNbO_3$ and $LiTaO_3$, *Phys. Rev.*, 1968, **167**, 314–319.

126 N. F. Evlanova, L. S. Kornienko and L. N. Rashkovich, EPR of some rare-earth ions and Cr^{3+} in $LiNbO_3$, *JETP*, 1967, **53**, 1920–1926.

127 L. Rebouta, M. F. da Silva, J. C. Soares, D. Serrano, E. Diéguez, F. Agulló-López and J. Tornero, Nonaxial sites for Er in $LiNbO_3$, *Appl. Phys. Lett.*, 1997, **70**, 1070–1072.

128 T. Bodziony and S. M. Kaczmarek, EPR study of low symmetry Er centers in congruent lithium niobate, *Phys. Status Solidi B*, 2008, **245**, 998–1002.

129 S. M. Kaczmarek and T. Bodziony, Low symmetry centers in $LiNbO_3$ doped with Yb and Er, *J. Non-Cryst. Solids*, 2008, **354**, 4202–4210.

130 T. Nolte, T. Pawlik and J.-M. Spaeth, EPR study of Er^{3+} in congruent $LiNbO_3$, *Solid State Commun.*, 1997, **104**, 535–539.

131 G. Malovichko, V. Grachev, J. Jorgensen, M. Meyer, M. Munro, B. Todt, I. Vrable, E. Kokanyan, V. Bratus and S. Okulov, Magnetic Resonance Study of Non-Equivalent Centers Created by 4f-Ions in Congruent and Stoichiometric Lithium Niobate, *MRS Proc.*, 2008, **1111**, 1111-D01–03.

132 G. Malovichko, V. Bratus1, V. Grachev and E. Kokanyan, Electron paramagnetic resonance and electron-nuclear double resonance of nonequivalent Yb^{3+} centers in stoichiometric lithium niobate, *Phys. Status Solidi B*, 2009, **246**, 215–225.

133 C. Bonardi, C. J. Magon, E. A. Vidoto, M. C. Terrile, L. E. Bausa, E. Montoya, D. Bravo, A. Martin and F. J. Lopez, EPR spectroscopy of Yb^{3+} in $LiNbO_3$ and $Mg:LiNbO_3$, *J. Alloys Compd.*, 2001, **323–324**, 340–343.

134 M. Nakamura, S. Higuchi, S. Takekawa, K. Terabe, Y. Furukawa and K. Kitamura, Optical Damage Resistance and Refractive Indices in Near-Stoichiometric MgO-Doped $LiNbO3$, *Jpn. J. Appl. Phys.*, 2002, **41**, L49–L51.